

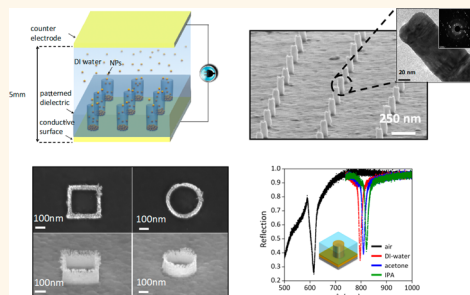
Three-Dimensional Crystalline and Homogeneous Metallic Nanostructures Using Directed Assembly of Nanoparticles

Cihan Yilmaz,[†] Arif E. Cetin,[‡] Georgia Goutzamanidis,[†] Jun Huang,[†] Sivasubramanian Somu,[†] Hatice Altug,^{‡,§} Dongguang Wei,[‡] and Ahmed Busnaina^{†,*}

[†]NSF Nanoscale Science and Engineering Center for High-Rate Nanomanufacturing (CHN), Northeastern University, Boston, Massachusetts 02115, United States,

[‡]Photonics Center and Department of Electrical and Computer Engineering, Boston University, Boston, Massachusetts 02215, United States, [§]Bioengineering Department, Ecole Polytechnique Federale de Lausanne (EPFL), Lausanne CH-1015, Switzerland, and [‡]Carl Zeiss Microscopy, One Zeiss Drive, Thornwood, New York 10594, United States

ABSTRACT Directed assembly of nano building blocks offers a versatile route to the creation of complex nanostructures with unique properties. Bottom-up directed assembly of nanoparticles have been considered as one of the best approaches to fabricate such functional and novel nanostructures. However, there is a dearth of studies on making crystalline, solid, and homogeneous nanostructures. This requires a fundamental understanding of the forces driving the assembly of nanoparticles and precise control of these forces to enable the formation of desired nanostructures. Here, we demonstrate that colloidal nanoparticles can be assembled and simultaneously fused into 3-D solid nanostructures in a single step using externally applied electric field. By understanding the influence of various assembly parameters, we showed the fabrication of 3-D metallic materials with complex geometries such as nanopillars, nanoboxes, and nanorings with feature sizes as small as 25 nm in less than a minute. The fabricated gold nanopillars have a polycrystalline nature, have an electrical resistivity that is lower than or equivalent to electroplated gold, and support strong plasmonic resonances. We also demonstrate that the fabrication process is versatile, as fast as electroplating, and scalable to the millimeter scale. These results indicate that the presented approach will facilitate fabrication of novel 3-D nanomaterials (homogeneous or hybrid) in an aqueous solution at room temperature and pressure, while addressing many of the manufacturing challenges in semiconductor nanoelectronics and nanophotonics.



KEYWORDS: directed assembly · nanoparticles · dielectrophoresis · 3-D nanostructures · nanoscale interconnects · plasmonic-based biosensing

Nanostructures with complex geometries and three-dimensional (3-D) architectures have recently received considerable interest in many fields, including electronics,¹ optics,² energy³ and biotechnology,⁴ since they enable superior device performance and miniaturization. Most approaches for fabricating these nanostructures rely on vacuum-based thin film deposition or electroplating, which requires a seed layer and many chemical additives. Directed assembly of nanoparticles (NPs) has been shown to be a promising alternative approach for building functional nanomaterials and nanostructures in aqueous solutions at room temperature and pressure.^{5–10} Much

progress has been made in assembling NPs into one, two and three-dimensional nanostructures by utilizing electric,^{7,11,12} magnetic⁹ and fluidic forces.¹³ However, there is a dearth of studies on fabricating crystalline, solid and homogeneous nanostructures. This is mainly due to the difficulties in controlling the assembly and fusion of NPs into desired geometries. Depending on the particle composition, functionalization and size, the forces and energies governing the assembly and fusion of NPs can be different. For example, on the basis of the suspension medium, NPs could possess different surface properties such as surface energy and charge, which can affect the assembly process and

* Address correspondence to busnaina@coe.neu.edu.

Received for review January 6, 2014 and accepted April 16, 2014.

Published online April 16, 2014
10.1021/nn500084g

© 2014 American Chemical Society

the NPs interaction with the substrate.¹⁴ Similarly, larger size NPs have higher melting temperature compared to smaller ones¹⁵ making them difficult to fuse into solid structures. To successfully fabricate nanostructures with the desired material and geometry, it is essential to identify the governing parameters that control the forces involved in the assembly process.

In this work, we developed a directed assembly technique that enables assembly and fusion of various metallic NPs to fabricate highly organized 3-D crystalline, solid nanostructures on surfaces. In this technique, colloidal NPs are assembled and simultaneously fused into 3-D nanostructures using an externally applied electric field. Using this method, we fabricated 3-D nanostructures made from gold, copper, aluminum and tungsten with feature sizes as small as 25 nm in less than a minute at room temperature and pressure without the need for a seed layer and chemical additives. The control of nanostructure dimensions was investigated as a function of many governing parameters such as voltage, frequency, assembly time and particle concentration. Material and electrical characterizations revealed that fabricated gold nanostructures have polycrystalline nature and very low resistivity ($1.96 \times 10^{-7} \Omega \cdot \text{m}$). The fabricated solid 3-D nanostructures also demonstrate high optical quality supporting strong plasmonic resonances with line-widths as narrow as 13 nm. This enables highly sensitive plasmonic-based biosensing of proteins.

RESULT AND DISCUSSION

Fabrication of 3-D Nanostructures. The fabrication process involves directing the assembly of colloidal NPs, using dielectrophoresis (DEP),¹⁶ onto a substrate. The substrate consists of a conductive film coated by any patterned insulator [e.g., poly(methyl methacrylate), PMMA or SiO_2] that features nanoscale patterns such as *vias*, trenches or other geometries as shown in Figure 1a. An AC electric field is applied between the substrate (through the exposed conductive film in the *vias*) and a counter electrode positioned approximately 5 mm from the substrate in the NP suspension. The electric field creates a dielectrophoretic force on the NPs, moving them toward the *vias* where the magnitude of electric field is highest (see Supporting Information Figure S1). The NPs under the effect of DEP also experience a pearl-chaining force,¹⁷ which plays an important role in assembling the NPs into the *vias*. The chaining force arises from the interaction of induced dipoles between the NPs. In addition, the surface charge of the particles would also create an additional induced dipole moment in the ionic atmosphere.¹⁸ The particle–particle interaction becomes very important when the NPs accumulate on the bottom surface of the *vias* allowing the NPs to attach to already-assembled NPs. As the NPs assemble, the applied electric field induces their fusion, forming arrays of solid nanostructures (Figure 1b). The fusion of

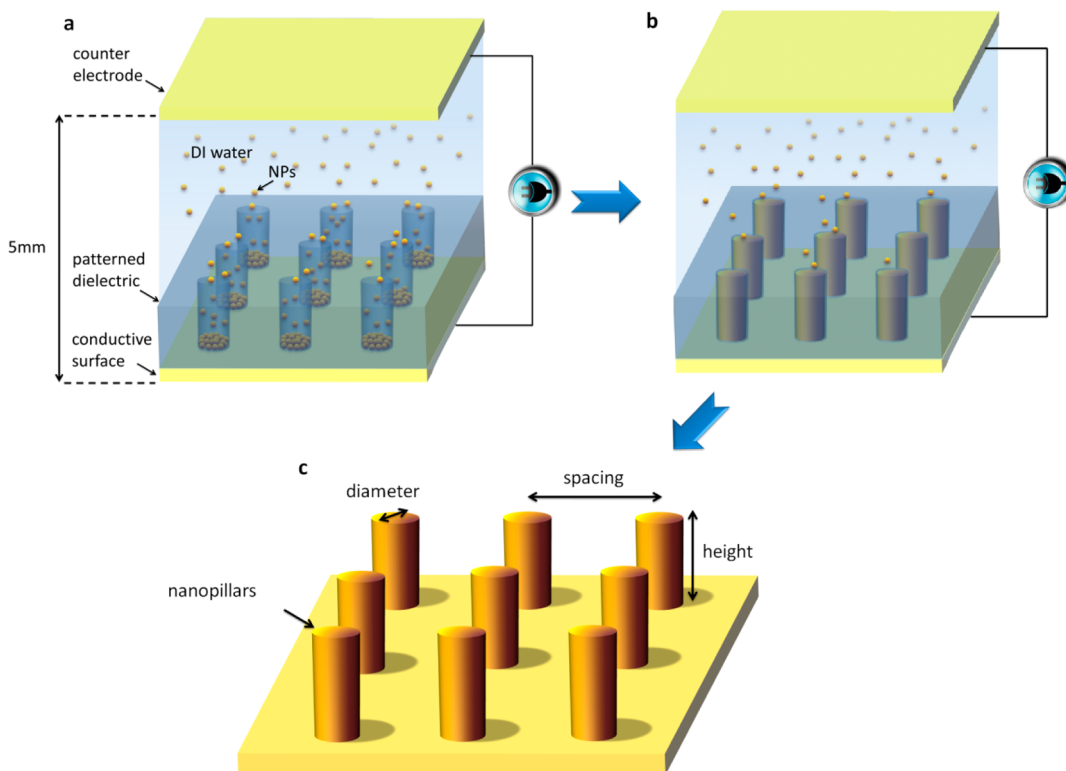


Figure 1. Fabricating 3-D nanostructures through electric field-directed assembly of NPs. (a,b) NPs suspended in aqueous solution are (a) assembled and (b) fused in the patterned via geometries under an applied AC electric field. (c) Removal of the patterned insulator film after the assembly process produces arrays of 3-D nanostructures on the surface.

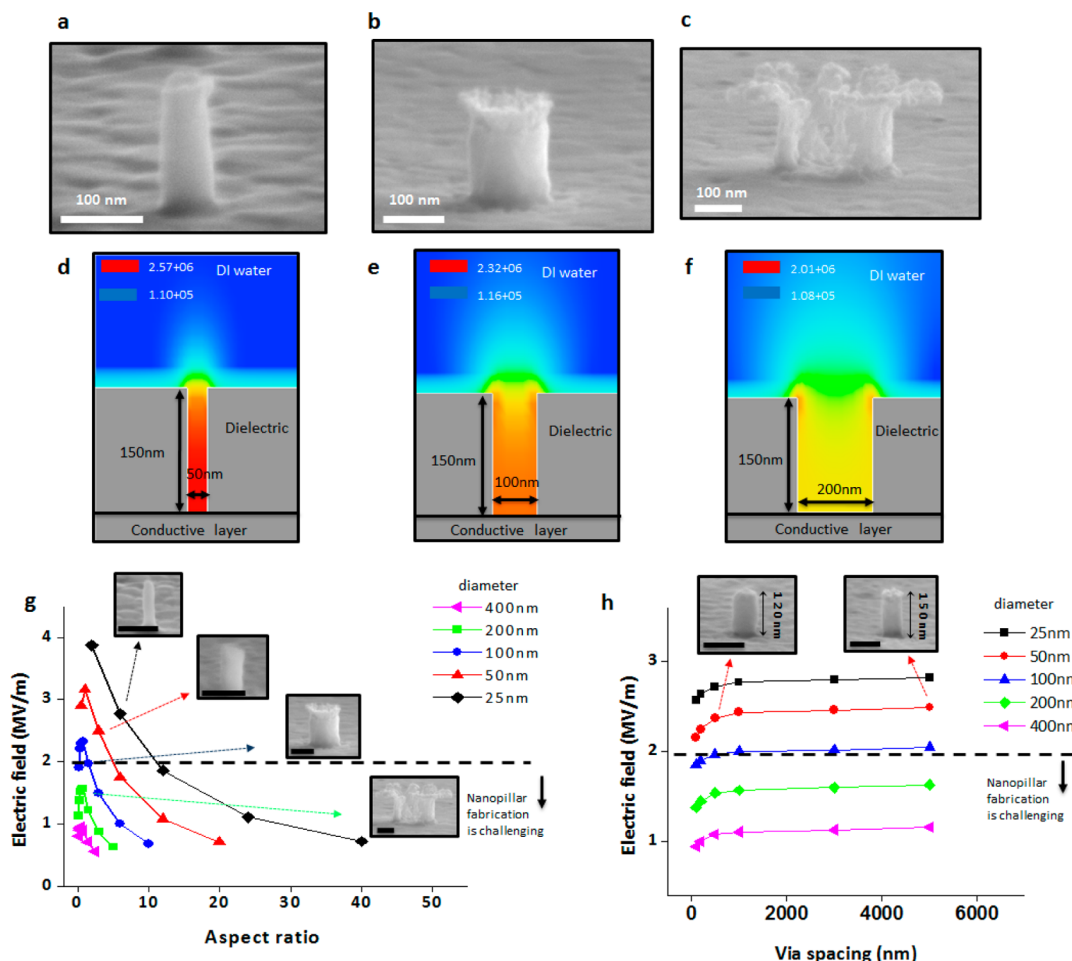


Figure 2. Effect of *via* geometries on nanopillar formation. (a–c) SEM images of (a) 50, (b) 100, (c) 200 nm-wide nanopillars. The nanostructure height is 150 nm. (d–f) Cross-sectional view (from the 3-D simulation) of different size *via*s, revealing the simulated localized electric field. (g) Electric field intensity in the *via* (at the center of the *via*) as a function of the aspect ratio (depth/diameter) for different *via* diameters. The spacing between the *via*s is 1 μm in these simulations. (h) Electric field intensity in the *via* (at the center of the *via*) as a function of the spacing between the *via*s. The *via* depth was 150 nm in these simulations. The scale bars in the inset figures in (g) and (h) are 100 nm.

small colloidal chains into structures such as wires under an applied electric field arises from localized Joule's heating, induced by the applied AC voltage at the NP junctions.¹⁹ Following the assembly and fusion process, the insulator layer can be removed (if needed) to obtain free-standing 3-D nanostructure such as nanopillars as shown in Figure 1c.

Effect of Pattern Geometry. The effect of pattern geometry (*via*s) on the nanopillar formation is shown in Figure 2. When the diameter of the *via*s are small, such as 50 and 100 nm, the 5 nm gold NPs successfully assemble and fuse into solid nanostructures at room temperature under the application of 12 V_{pp} AC voltage with a frequency of 50 kHz for 90 s (Figure 2a,b). Since gold NPs (or any conductive NPs) are highly polarizable, they are attracted toward the *via*s where the electric field intensity is high with a DEP force of 4.51×10^{-14} N (see Supporting Information pp 2–5). However, when the *via* diameter was increased to 200 nm, only partial assembly was observed in the *via* (under the same experimental conditions used to

fill sub-100 nm diameter *via*), resulting in an incomplete nanopillar formation (Figure 2c). This maybe due to the electric filed intensity and distribution in the *via*s. To fully understand this phenomenon, we used 3-D computational fluid dynamics simulation to model the electric field near the *via*. The simulation results show that the intensity of the electric field in the *via*s varies depending on the geometrical parameters such as diameter, depth and *via* spacing. Figure 2d–f displays the static electric field contours in a *via* for three different *via* diameters for a fixed depth and spacing (for the same dimensions shown in Figure 2a–c). The electric field intensity at the center of the *via* decreases as the diameter increases. This results from the amplification of the electric field only at the edges of the patterns.²⁰ For a *via*-shaped geometry, the electric field strength is always higher at the side-walls compared to the center. This effect is not significant in small *via*s because the side-walls are much closer. When the diameter becomes sufficiently large, the center part of the *via* is not affected by the amplification of the

electric field at the side-wall, leading to lower field intensities at the center. Therefore, NPs are exposed to smaller DEP forces at the center of a large *via*, resulting in only partial particle assembly. The calculated DEP force acting on a 5 nm particle located 230 nm away from the bottom (measured from the center) of a 200 nm diameter *via* is 1.54×10^{-14} N. This force is three times smaller than the DEP force at the same distance from a 50 nm diameter *via* (see Supporting Information p 5), explaining the incomplete assembly results shown in Figure 2c.

The intensity of the electric field for *vias* with various aspect ratios and fixed spacing is presented in Figure 2g. As the aspect ratio of the *vias* increases, the electric field intensity decreases because of the fact that larger aspect ratio *viyas* are less affected by the electric field amplification at the edge of the *via* (see Supporting Information Figure S2). To demonstrate the effect of the aspect ratio on the nanopillar formation and make a systematic comparison, we assembled 5 nm gold particles into *viyas* with aspect ratios of 6, 3, 1.5, and 0.75 and 1 μ m spacing that were simulated in Figure 2g. The experimental conditions were 12 V_{pp} AC voltage with a frequency of 50 kHz for 90 s. The results showed that when the electric field in the *viyas* (at the center of the *via*) falls substantially below 2×10^6 V/m, the DEP force on the NPs becomes so low that only partial nanopillar formation is observed (Figure 2g inset SEM images). For example, the simulation shows that the *viyas* with aspect ratios of 1.5, 3, and 6 have electric field intensities at or higher than 2×10^6 V/m. In these cases, NPs successfully assemble in the *via* forming solid nanopillars. On the other hand, for the *via* with aspect ratio of 0.75, the electric field intensity at the center is 1.56×10^6 V/m resulting in an incomplete nanopillar formation. The NPs were assembled only at the side-walls where the electric field intensity was $\sim 2 \times 10^6$ V/m (Figure 2f). These simulation and experimental results indicate that for a complete nanopillar formation using the aforementioned experimental conditions, the electric field intensity in the *via* should be equal or larger than 2×10^6 V/m.

The simulations in Figure 2h show that, for a given *via* diameter and depth, the electric field intensity in the closely spaced *viyas* was small compared to the sparsely spaced *viyas* (see Supporting Information Figure S3). This would lead to a lower nanopillar height in closely spaced *viyas*. To demonstrate this, we assembled 5 nm gold particles into 50 nm diameter and 150 nm deep *viyas* separated with 500 and 5000 nm under 12 V_{pp} AC voltage with a frequency of 50 kHz for 90 s. As shown in the inset images in Figure 2h, the closely spaced nanopillars were shorter (120 nm) than the sparsely spaced nanopillars (150 nm) due to the lower electric field and consequently smaller DEP force exerted on the NPs near these *viyas*. The simulations and experiments discussed above indicate that the

simulation results presented in the Figure 2g,h will be useful for estimating the assembly outcome and nanopillar formation for various *via* dimensions.

Control of the Fabrication Process. The results show that the amplitude and frequency of the applied voltage can be controlled to achieve a successful nanopillar formation for different *via* geometries. Typically, 50 nm diameter pillars can be obtained when the voltage is applied at 12 V_{pp} with a frequency of 50 kHz for 90 s. When a lower voltage (~ 6 V_{pp}) is applied, the DEP and chaining forces decrease, resulting in a partially assembled and partially fused particles in the *viyas* (see Supporting Information Figure S4a). On the other hand, the application of a higher voltage (~ 20 V_{pp}), significantly increased the assembly rate but resulted in undesirable particle over assembly and agglomeration on the PMMA surface (see Supporting Information Figure S4b). Similarly, the NP assembly in the *viyas* could also be controlled by varying the frequency of the applied field. At higher frequencies (~ 100 kHz), the counterions on the particles can not follow the rapidly oscillating electric field,¹⁸ which decreased the particle–electric field interaction and the assembly rate (see Supporting Information Figure S4c), whereas at low frequencies (~ 10 kHz), the assembly rate became very high, once again leading to undesirable particle over assembly and agglomeration in localized regions mostly near the edges of the *via* array (see Supporting Information Figure S4d). Therefore, the applied voltages need to be slightly higher than 12 V_{pp} (14–16 V_{pp}) at lower frequencies (30–50 kHz) to efficiently assemble nanostructures in large diameter (>50 nm) *viyas*.

As discussed earlier, when the *via* diameter is at or larger than 200 nm, the electric field and DEP force near the *viyas* becomes so low that complete nanopillar formation using only AC voltage becomes difficult. To achieve a successful particle assembly and chaining in the *viyas*, the DEP force needs to be above a certain threshold in addition to having a sufficient particle concentration near the *viyas*.¹⁸ Since the DEP forces are only effective within a few hundred nanometers,²¹ manipulation of AC voltage was not sufficient to achieve complete nanopillar formation in these large *viyas*. To overcome this, we applied a constant DC offset voltage in addition to the AC voltage. The DC voltage creates an additional electrophoretic (EP) force on the NPs that will drive the NPs closer to the substrate and effectively increase the particle concentration in the vicinity of the *viyas*. This can be further demonstrated by the fact that the magnitude of electrophoretic force on 5 nm gold NPs under a DC voltage of 2 V is 1.78×10^{-12} N, which is almost 2 orders of magnitude higher than the DEP force. As a result, a uniform nanopillar formation in 200 nm diameter *viyas* is achieved (see Supporting Information pp 9–10 and Figure S5). Table 1 summarizes the critical assembly parameters

and their ranges used for the fabrication of metallic nanostructures with different dimensions.

Fusion Mechanism. The fusion of NPs into solid nanostructures results largely from Joule's heating at the nanoparticle interface due to the applied current.^{19,22,23} To estimate the Joule's heating at the particle-surface interface, we used the model shown in Figure 3a. In this model, the NP temperature increase due to Joule's heating ΔT can be calculated by $\Delta T = Q/(v \cdot c_{v,p})$ where v is the particle volume, $c_{v,p}$ is the specific heat capacity of NPs, and Q is the Joule's heating, which can be determined by $Q = I_p^2 \cdot R_c \cdot t$ where I_p is the magnitude of the current passing through a nanoparticle, R_c is the

contact resistance at the particle-surface interface, and t is the time period of the applied current. The contact resistance is $R_c = (\rho_c \cdot z_0)/A_c$ where ρ_c is at the particle-surface interface, z_0 is separation distance between the particle and the surface, and A_c is the contact area which is function of contact radius a . Therefore, ΔT can be expressed as follows (see Supporting Information pp 10–16 for the detailed derivations):

$$\Delta T = \frac{3I_p^2 \rho_c z_0 t}{4\pi^2 c_{v,p} a^2 r^3} \quad (1)$$

To calculate ΔT using this equation, the contact radius, the contact resistivity and the current passing through a nanoparticle need to be determined. The contact radius can be calculated from adhesion-induced deformation of NPs. Our calculations showed that the NPs plastically deform under van der Waals force F_a . Therefore, we used Maugis and Pollock (MP) model in plastic deformation²⁴ to determine contact radius of different size of NPs. (see Supporting Information pp 11–12 for calculations). It has been reported that the resistivity of metals at nanoscale dimensions is higher than their bulk resistivity^{25–27} because of electron scattering from grain boundaries and interfaces.^{27,28} For example, Ramsperger *et al.*²⁵ showed that the electrical resistivity of a 4 nm wide and 1 nm thick gold nanowire is 1.5×10^{-4} ohm·m, which is 6 orders of magnitude higher than bulk gold resistivity. Similarly,

TABLE 1. Summary of the Parameters Affecting Metallic 3-D Nanostructure Fabrication Process for Different *Via* Diameters with a Fixed *Via* Depth at 150 nm

parameter	range	
	<i>via</i> diameter <200 nm	<i>via</i> diameter ≥ 200 nm
voltage	12–16 V _{pp}	16–20 V _{pp}
frequency	30–70 kHz	30–70 kHz
DC voltage	—	2 V
assembly time	30–90 s	60–120 s
particle size	≤ 10 nm	>20 nm
particle concentration	$\sim 10^{13}$ mL ⁻¹	$>10^{14}$ mL ⁻¹
postcurrent applied	—	>5 mA

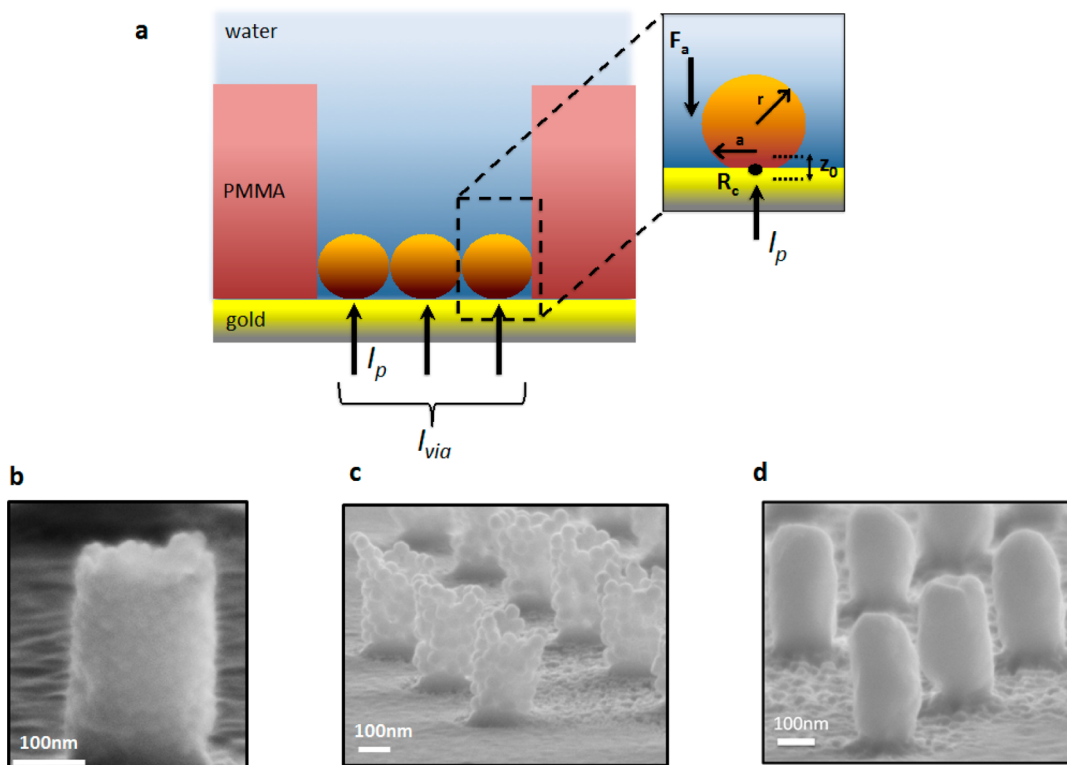


Figure 3. Fusion of NPs into solid nanostructures. (a) Schematic of the model used for fusion calculations. (b,c) Tilted SEM images of 200 nm diameter nonfused nanopillars fabricated using (b) 20 and (c) 50 nm gold NPs. (d) Fused nanopillars after 10 mA DC current is passed through the nanopillars in (c).

Celleja *et al.*²⁶ obtained a resistivity of 3×10^{-7} ohm·m from a 40 nm diameter gold wire, and Zou *et al.*²⁷ obtained a resistivity of 7×10^{-8} ohm·m from a 75 nm diameter gold wire. Therefore, bulk resistivity of gold cannot be used in eq 1. To determine the resistivity at the nanoparticle-surface interface ρ_c , we interpolated the reported resistivity values above. The RMS value of AC current was measured using an ammeter at an applied AC voltage of 12 V_{pp} at 50 kHz with a 2 V DC offset. To estimate the current passing through a particle I_p , the amount of current passing through a *via* (I_{via}) was determined by subtracting the current passing through the entire chip without patterned *vias* (just a PMMA film) from total current measured after the *vias* were patterned. Then, the resulting current was divided to the number *vias* and then to the number of monolayer particles in a single *via* (Figure 3a).

Our calculations showed that the temperature of 5 nm gold particles increases by 593 °C during the assembly process under the applied voltage of 12 V_{pp} (measured current is ~1.62 mA). Since small size particles have much lower melting temperature compared to their bulk melting points,¹⁵ this temperature would fuse 5 nm gold particles into solid nanostructures. This explains the formation of solid nanopillars shown in Figure 2a,b. As eq 1 shows, ΔT decreases as a function of r^3 leading to a much smaller temperature increase for larger size particles. According to our calculations, the temperature of 20 and 50 nm particles increase by 63.1 and 3.23 °C, respectively, which are insufficient for complete particle fusion. To verify these calculations, we assembled 20 and 50 nm gold particles. We applied an AC voltage of 12 V_{pp} at 50 kHz with a 2 V DC offset during 90 s for all experiments. It is evident from the SEM images in Figure 3b,c that 20 nm particles were partially fused and 50 nm gold particles were nonfused, as it was predicated in the calculations. However, we showed that the partially fused or non-fused NPs can be completely fused into solid nanopillars by passing a high current following the assembly process. Figure 3c shows the SEM images of solid nanopillars made from 50 nm particles after a 10 mA post-DC current is applied during 120 s. To calculate the temperature increase for this case, we modified the previous model shown in Figure 3a as follows: (1) we assumed that the current passes through the series of particles assembled perpendicularly in the *via*, (2) we used the particle-particle contact radius instead of particle-substrate contact, and (3) we updated the time period required for fusion (see Supporting Information Figure S10). The modified model results showed that the temperature of the assembled 50 nm particles increases by 477 °C, explaining the complete fusion of these NPs into solid nanostructure. The calculations and experiments indicate that as the size of NPs increases, complete fusion into solid nanopillars does not occur without applying postcurrent

treatment. For a solid nanopillar formation using larger size NPs (>20 nm), a high current (>5 mA) should be applied through the NPs following the assembly process.

Capabilities of the Fabrication Technique. Control of the governing parameters enabled successful fabrication of nanopillars down to 25 nm with controlled dimensions and various materials, over large areas (Figure 4). The fabricated nanopillar arrays showed good uniformity over a large area. For example, the average height of 35 nanopillars measured at different locations of 1 mm × 1 mm nanopillar arrays was 117.5 nm with uniformity of 90.3% (see Supporting Information Figure S11). The nanopillars in the corner of the arrays were taller than the ones in the center because of the electric field edge effect.²⁰ When the nanopillars in the corners were excluded, the uniformity increased to 94.5%. The high magnification microscopy images in Figure 4b–d indicate that the fabricated nanopillars have smooth side walls for all dimensions fabricated, indicating the fusion of the NPs. Using the presented directed assembly approach, any other metallic NPs can be fabricated on any conductive surface. Figure 4e–g shows fabrication of nanopillars from copper, aluminum, tungsten NPs. In addition, the preliminary results show that it is possible to make hybrid nanostructures by sequentially assembling other types of inorganic or organic NPs such as silicon and polystyrene-latex (PSL). Figure 4h shows the SEM image of a 50 nm diameter gold–silicon hybrid nanopillar fabricated by assembling 5 nm silicon NPs on a gold nanopillar formed at the bottom of the *via*. The height of the gold portion of the nanopillar was controlled by adjusting the assembly time. Similarly, Figure 4i shows the SEM image of a gold-fluorescent PSL hybrid nanostructure fabricated by assembling 22 nm fluorescent PSL NPs on top of a gold nanopillar. The resulting hybrid nanostructure is clearly shown by the fluorescent microscopy images in Figure 4i inset. In addition to nanopillars, we also demonstrate the fabrication of complex 3-D nanostructures such as nanorings and nanoboxes as shown in Figure 4j. These nanobox geometries have a larger exposed area and lower electric field than those of the 50 nm diameter *via* geometries presented in Figure 2a (see Supporting Information Figure S12). To fabricate these structures, we applied a higher voltage (16 V_{pp}) and a lower frequency (30 kHz) for 90 s to assemble 5 nm gold particles. Ring shape nanostructures are important for spintronics application, such as magnetoresistive random access memory (MRAM).²⁹ Cost-effective fabrication of these nanostructures from various materials with precise control of dimensions is strongly desirable for practical applications. In this work, we demonstrate that we can fabricate ring and box shape structures with a thickness down to 25 nm without using complex or multiple fabrication steps.

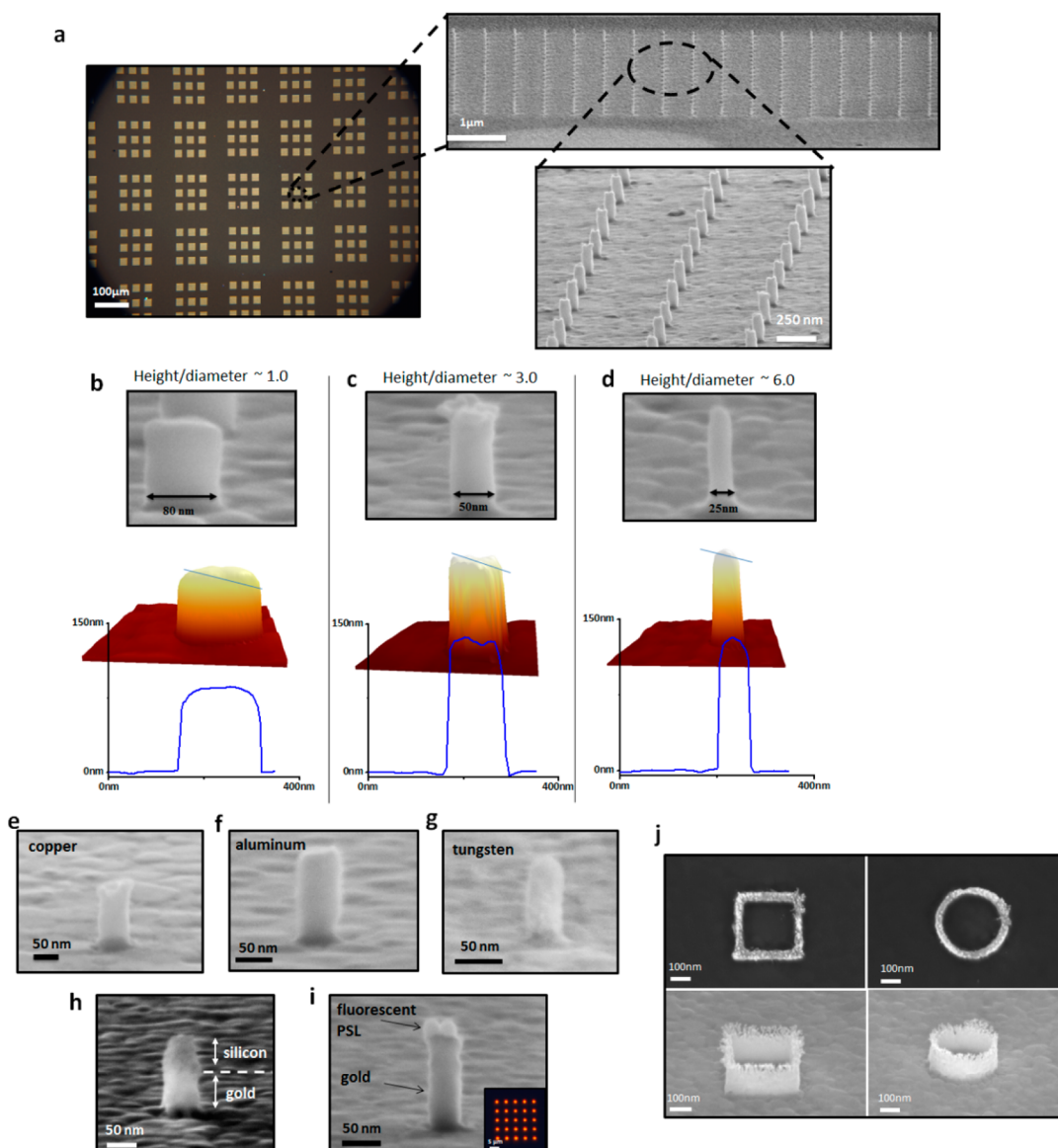


Figure 4. Capability of NP assembly process for fabricating various sizes, types, and shape of 3-D nanostructures. (a) Optical microscopy image of nanopillar arrays fabricated over 1×1 mm area. Insets show close-up SEM images of gold nanopillar arrays from a single array (area: $10 \mu\text{m} \times 10 \mu\text{m}$). (b–d) SEM images of individual gold nanopillars with various aspect ratios, which were confirmed in corresponding atomic force microscopy (AFM) images. (e–g) Fabricated nanopillars made of (e) copper, (f) aluminum, (g) tungsten, (h) gold and silicon, (i) gold and fluorescent PSL. Inset in (i) shows fluorescent images after PSL NPs are assembled on the gold nanopillar. (j) Top-down and high-angle SEM images of a 3-D nanobox (left) and a nanoring (right) fabricated using dielectrophoretic NP assembly.

Material Properties. We used transmission electron microscopy (TEM) to determine the material characteristics of our fabricated gold nanopillars, which were placed on a copper TEM grid using a conventional lamella lift-out process (see Supporting Information pp 19–20, Figure S13). The bright-field image in Figure 5a indicates that the gold NPs were completely fused during the assembly process, transforming them into homogeneous nanopillars without any voids or gaps. The small-area electron diffraction (SAED) pattern obtained from the entire nanopillar presented in the inset to Figure 5a revealed the polycrystalline nature of the nanopillars (see Supporting Information Figure S14). Notably, only

two grains, each having its lattice orientation in one direction, existed over the $30 \text{ nm} \times 30 \text{ nm}$ area of the nanopillar (Figure 5b). Recalling that the nominal diameter of an individual NP was 5 nm, we infer that large number of NPs fused into a single grain. The formation of a single-crystalline material might have resulted from the recrystallization of multiple NPs during the fusion process.³⁰

Electrical Properties. To demonstrate that fabricated nanostructures have promises in nanoelectronics, we compared the electrical characteristics of our fabricated nanopillars with those of nanopillars fabricated by a conventional electroplating process using an

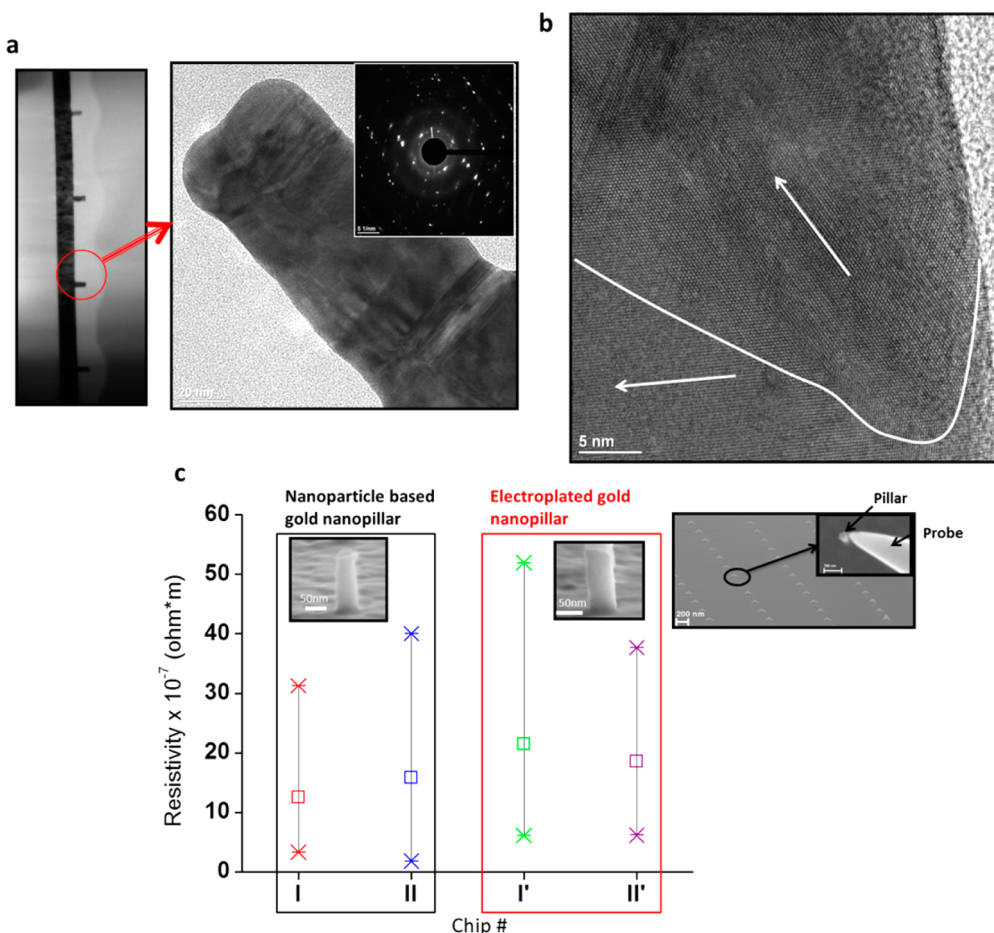


Figure 5. Material and electrical characterization of the nanopillars. (a) Bright-field TEM image of NP-based gold nanopillars; inset: diffraction pattern of the pillar. (b) High-resolution TEM image, indicating the existence of two grains within the 30 nm \times 30 nm area of a single nanopillar. Arrows indicate the two different lattice directions. (c) Resistance measurements of the electroplated and NP-based gold nanopillars (diameter: 50 nm, height: 150 nm), 10 nanopillars from two different chips each. Inset shows high-angle SEM image of gold nanopillars in the PMMA during the electrical characterization.

SEM-based *in situ* Zyvex S-100 nanomanipulator (see Supporting Information pp 20–27, Figures S15 to S19). Both the NP-based and electroplated gold nanopillars yielded comparable resistance (Figure 5c). On the basis of our measurements, the lowest resistivity (calculated) for 20 different NP-based pillars is $1.96 \times 10^{-7} \Omega \cdot \text{m}$, which is only an order of magnitude higher than the bulk resistivity of gold ($2.44 \times 10^{-8} \Omega \cdot \text{m}$) (see Supporting Information Figure S19). This is attributed to the nanoscale dimensions of the nanopillars. As mentioned earlier, when the dimensions of metals are comparable with or less than the mean free path (~ 30 nm for gold), the resistivity of metals become higher than their bulk resistivity^{25–27} because of electron scattering from grain boundaries and interfaces.^{27,28} The obtained resistivity value is even lower compared to some of the previously obtained values of resistivity for electroplated or vacuum-deposited gold nanowires having similar dimensions.^{31,32} Moreover, flexibility in material choice of our method provides additional benefits over electroplating. Although electroplating has the advantages of being simple and cost-effective in

general, not every metal can be electroplated on any conductive surface.^{33,34} This makes electroplating limited in terms of the number of structures that can be fabricated on desired surfaces.³³ In addition, in some cases, electroplating process involves the use of seed layers and many chemical additives^{35,36} which could increase the complexity and the cost involved in the process. Because the formation of the nanopillars in our process is governed by the physical assembly followed by fusion of NPs on the surface and not by the chemical nucleation as in electroplating, any conducting materials can be directly fabricated on surfaces without requiring an intermediate seed layer or chemical additives. We also showed that nanopillar formation rate of our directed assembly process is as fast as electroplating for the same nanopillar geometry, density and area (see Supporting Information Figure S15). This together with the scalability of the presented process, for example, could pave the way for seedless copper interconnect technology³⁷ and fabrication of very-small-diameter (<16 nm) interconnects,³⁸ which are difficult challenges in CMOS

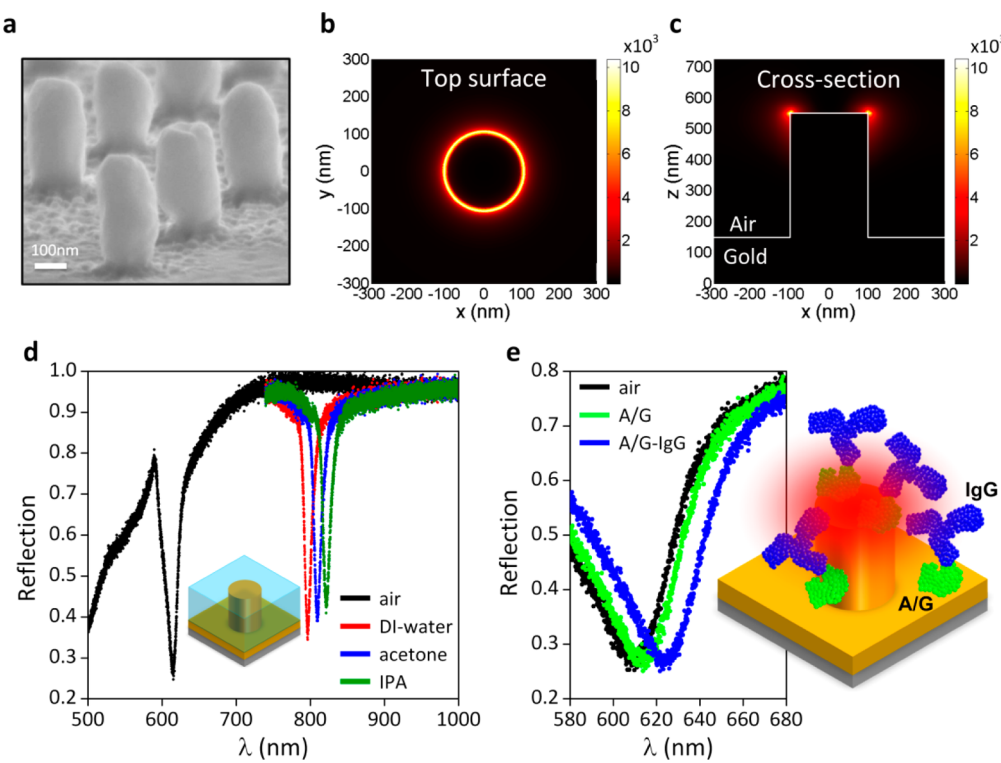


Figure 6. Demonstration of the sensitivity of the fabricated nanopillars. (a) SEM image of the fabricated nanopillar structures. **(b,c)** Near-field intensity enhancement distributions calculated **(b)** at the top surface of the nanopillar and **(c)** through cross-section. **(d,e)** Variations in the spectral response of the nanopillar arrays **(d)** after introducing bulk solutions with different refractive indices: DI-water $n_{\text{DI}} = 1.333$, acetone $n_{\text{acetone}} = 1.356$, and IPA $n_{\text{IPA}} = 1.377$, and **(e)** after attachment of 1 mg/mL of A/G and 1 mg/mL of IgG.

(complementary metal–oxide–semiconductor) based manufacturing.

Optical Properties. The presented fabrication technique also enables high quality plasmonic nanostructures for optical device applications. Plasmonics has recently received significant attention since surface plasmons (SPs), by localizing and enhancing light at a metal/dielectric interface, lead strong light/matter interactions.³⁹ Advances in plasmonics, however, strongly depend on the ability to pattern high quality metals and hybrid materials at nanoscale dimensions. In recent years several new fabrication approaches have been proposed to exploit plasmons for wide range of applications.^{40,41} One promising application of plasmonics is biosensing.^{42–44} Biosensing platforms utilize plasmonic resonances that show variations due to change in the refractive index of their surrounding medium. To achieve a reliable biosensor with low limit of detection, narrower resonances and high overlap between optical fields of the plasmonic mode and the interacting biomolecules is needed. Recently, a plasmonic metamaterial structure based on randomly positioned nanopillar arrays are shown to be highly suitable for ultrasensitive biosensing by Kabashin *et al.*⁴ We numerically analyzed a periodic nanopillar system to further improve biosensing performance.⁴⁵ As shown in Figure 6a, the optimized nanopillars have diameter and height, roughly 200 and 400 nm,

respectively. These nanostructures with such high aspect ratio are challenging using lift-off based electron-beam lithography techniques. Figure 6b,c shows the near-field intensity enhancement ($|E|^2/|E_{\text{in}}|^2$) distribution at the top surface and through cross section, respectively. Our numerical calculations indicate that nanopillar arrays enhance the incident light intensity up to 10 000 times. More importantly, these large local fields extend deep into the medium making them easily accessible to monitor changes in their surrounding medium (see Supporting Information pp 27–28). This strongly amplifies the sensitivity of the nanopillar based plasmonic nanosensors to determine the local refractive index changes. For experimental demonstration we fabricated well-defined periodic nanopillar arrays using our new nanofabrication method. We found that fabrication of these large diameter and deep structures over a large area (over 0.2 mm area) is challenging using 5 nm particles, mainly because of very low electric field in the *vias* (see Supporting Information Figure S21). To overcome this, we carried out various modifications in the assembly conditions. First, we used 50 nm gold particles instead of 5 nm. Larger particles experienced larger DEP forces, which increased the assembly rate in the *vias*. Second, we applied a DC offset together with AC electric field during the assembly process. This not only increased the force on the particles but also led a uniform particle

assembly over the *via* array.⁴⁶ Third, we increased the assembly time to 10 min for tall structures with large diameter (400 nm height and 200 nm diameter). As mentioned earlier, these large particles were not fused during the assembly. Therefore, following the assembly, a high current (~10 mA) has been passed through these particles to fuse them into solid nanostructures (see Supporting Information Figure S21). The structures demonstrated high optical quality supporting strong plasmonic resonances with line-widths as narrow as 13 nm. The resonance strongly shifts with different refractive indices of bulk solutions including DI-water $n_{\text{DI}} = 1.333$, acetone $n_{\text{acetone}} = 1.356$, and IPA $n_{\text{IPA}} = 1.377$. As shown in Figure 6d, we demonstrate a refractive index sensitivity as large as 571 nm/RIU. Because of spectrally narrow resonances, we achieved an experimental figure of merit as large as 44. Nanopillar structures are also suitable for surface based biosensing, which is demonstrated by detecting protein monolayers (A/G) and bilayers (Immunoglobulin G (IgG) bind of A/G). As shown in Figure 6e, because of accumulation of biomass on the sensor platform, the plasmonic resonance shifts robustly with 4 and 14 nm after addition of protein A/G and IgG, respectively.

CONCLUSIONS

In this paper, we introduce a new aqueous directed assembly approach to fabricate crystalline, homogeneous and 3-D nanostructures with controlled dimensions. By identifying and controlling the driving forces of the assembly process, we demonstrated the ability of fabricating various metallic 3-D nanostructures with feature sizes as small as 25 nm. These metallic nanostructures have lower or equivalent electrical resistivity compared to electroplated gold, and support strong

plasmonic resonances. In addition, the fabrication process is as fast as electroplating, shown to be scalable to the millimeter scale and conducted at room-temperature and pressure without requiring chemical additives making it highly suitable for cost-effective, green nanomanufacturing.

The fabricated nanostructures can be used for a wide range of applications in the area of nanoelectronics and nanophotonics. For example, future generation CMOS circuits demand for very small size (<16 nm) and high aspect ratio interconnects.³⁸ According to the Semiconductor Industry Association's International Technology Roadmap for Semiconductors (ITRS),⁴⁷ fabrication of these structures using conventional electroplating or vacuum deposition is challenging. The ability to produce nanoscale structures with controlled dimensions through this method could enable fabrication of very small size interconnects from vastly different materials including copper, tungsten and silver.^{47,48} Nanopillars with specific dimensions (diameter, height and spacing) bring complementary characteristics of localized and extended surface plasmons together.⁴⁵ This could lead to plasmonic devices with multiple sensing modalities, including label-free biodetection, surface enhanced vibrational spectroscopy and optical trapping at the same time.^{45,49} Combining fluorescence NPs with metallic nano-objects could enable the control of optical emission characteristics. Similarly, the fabrication of layers of dielectric and metallic structures could be used as metamaterials with unique optical properties^{39,50} and hybrid plasmonic nanoantennas.^{51,52} In addition, hybrid structures made from semiconducting and metallic layers can find applications in hybrid electronics⁵³ and 3-D photovoltaics.³

MATERIALS AND METHODS

Particle and Substrate Preparation. The aqueous gold NPs suspension was purchased from British Biocell International (nominal diameter: 5 nm). NPs were directly used from commercial suspensions. The gold colloid is composed of chloroauric acid (<0.01%), sodium citrate (<0.00001%), tannic acid (<0.0000001%) and potassium carbonate (<0.0000001%) and have citrate stabilization with a net negative surface charge. The zeta potential of the gold particles and the conductivity of the suspension are -41 ± 7 mV and 600 $\mu\text{S}/\text{cm}$, respectively. The aqueous copper, tungsten, aluminum and silicon NPs suspension was purchased from Meliorium Technologies (nominal diameter: 10 nm). These NPs have sodium dodecylbenzenesulfonate functionalization. The zeta potentials of these particles varies between -45 mV and -50 mV. The conductivity of the suspensions is around 2 mS/cm. The aqueous fluorescent polystyrene-latex (PSL) NPs suspension was purchased from Thermo Scientific (Fluoro-Max Red, nominal diameter: 22 nm). The zeta potential of fluorescent PSL particles is -43 mV \pm 5 mV. The conductivity of the suspension is around 700 $\mu\text{S}/\text{cm}$. The original suspension was diluted in DI water 10–100 times prior to assembly.

The preparation of the substrates, displayed in Figure 1, began with Cr/Au (2 nm/120 nm) being sputtered onto a SiO₂/Si

(470 nm/380 μm) wafer, which was then diced into 12 mm \times 12 mm chips. Next, PMMA was spin-coated onto the precleaned (piranha: H₂SO₄/H₂O₂, 2:1) Cr/Au chips. The nanoscale patterns were fabricated using conventional electron beam lithography, with subsequent development in methyl isobutyl ketone and isopropyl alcohol (MIBK/IPA, 1:3).

NP-Based Nanopillar Fabrication. The substrate and a counter electrode (Cr/Au sputtered gold) were connected to a function/arbitrary waveform generator (Agilent 33220A) and submerged into the NP suspension. Following the application of a sinusoidal AC electric field with or without a DC offset, the substrate and the counter electrode were removed from the suspension using a dip coater (KSV NIMA) at a controlled speed (85 mm/min). Finally, the PMMA layer on the substrate was removed using acetone for metallic and silica nanopillars, ethanol for PSL nanopillars.

Nanopillar Electropolating Process. A Techni-Gold 25 ES RTU (ready-to-use) solution was purchased from Technic Inc., which includes sulfuric acid, ethylenediamine, sodium gold sulfite and sodium sulfite. The temperature of the solution was held at 60 °C. The substrate with patterned geometries and a counter electrode were submerged into the electroplating solution. In contrast to the directed assembly, a platinized titanium mesh was used as the counter electrode. A temperature probe was

inserted into the solution, which was heated at a set temperature of 60 °C, while a magnetic stirrer was set to a rate of 75 rpm. A DC voltage was applied, using a Keithley 2400 source meter, between the substrate and the counter electrode. The magnitude of the applied voltage and the deposition time were altered to control the electroplating rate.

Electrical Characterization. Electrical properties of the nanopillars were measured using an *in situ* NanoManipulator (Zyvex S-100). Three tungsten probes with a 20 nm-diameter tip were used to form the electrical contact. The manipulator probes were connected to an Agilent 4156C source measure unit. Initially, two of the probes contacted the bottom gold layer to measure the resistance of thin film. Once good contact was achieved between the two probes and the gold layer (resistance: ca. 10 Ω), a third probe was applied to a nanopillar. The resistance of the nanopillar was measured by activating one of the probes on the gold layer and the probe on the nanopillar.

TEM Sample Preparation. High-resolution TEM and selected-area diffraction were employed to characterize the fabricated nanopillars. A Zeiss Auriga focused ion beam/scanning electron microscopy (FIB-SEM) workstation was employed for preparation of the high-resolution TEM sample. To prepare a TEM specimen from a bulk wafer presenting the fabricated nanopillars, one array of nanopillars was coated with a carbon protection layer having a thickness of up to 1.5 μm. The carbon protection layer was formed using electron beam-assisted deposition for approximately the first 100 nm and then ion beam-assisted deposition was applied up to 1.5 μm. A lamella that contained the chosen array was cut out with various steps of FIB milling (recipes from the system). The lamella was then lifted out *in situ* and welded onto an Omniprobe Mo TEM grid using an Omniprobe Autoprobe 300 mounted on the roof of the FIB/SEM chamber. Once on the TEM grid, the lamella was further thinned down to approximately 100 nm using a 30-keV Ga ion beam. Final polishing and cleaning was performed using a 2-keV ion beam to minimize the ion beam damage to the nanopillars, resulting in lamellae having a final thickness of approximately 50–60 nm.

TEM Characterization. High-resolution TEM imaging and diffraction were performed using a 200 kV Zeiss Libra 200 field emission energy-filtering transmission electron microscope (FEG EF-TEM). All bright-field TEM images were acquired at 200 keV. SAED was achieved using a 10-μm condenser aperture, selectively illuminating the area of interest in the specimen.

Electric Field Simulation. The magnitudes of the electrical potential and electric field counters near the patterns were simulated using commercial 3-D finite-volume modeling software (FLOW-3D). In the simulations, the root-mean-square (RMS) value of the utilized voltage was applied to the gold layer beneath the vias. The calculated local electric field near the via was used to determine the electric field gradient, which was then used to calculate the DEP force on the particles.

FDTD Simulations. Three-dimensional finite-difference time-domain (3D-FDTD) simulations were carried out to numerically analyze the far- and near-field responses of the NP system. The permittivity of gold was taken from ref 33. In FDTD simulations, periodic boundary conditions were applied along the x- and y-directions and Perfectly Matched Layer (PML) boundary condition was applied along the direction of the illumination source, z. The mesh size was chosen to be 2 nm along the x-, y-, and z-directions.

Sensing Experiment Presentation. As a first step, nanopillars were immersed in ethanol solution for 30 min to remove the organic contamination on the surface. The protein monolayer was formed by spotting 1 mg/mL of A/G on the chip surface and incubating for 1 h. A/G is a recombinant fusion protein that consists of binding domains of both protein A and protein G. Protein A/G sticks on the gold surface by physisorption. Nanopillars were then rinsed with PBS (phosphate buffer) to remove the unbound proteins. The protein bilayer was formed by spotting 1 mg/mL of IgG on the chip surface and incubating for 1 h. Protein IgG is immobilized on A/G monolayer because of the high affinity of protein A/G to the Fc regions of IgG. Finally, a washing process was performed to remove the unbound protein.

Spectral Measurements. All spectral measurements were performed by a Nicon Eclipse-Ti microscope coupled to a SpectraPro 500i spectrometer. Normally incident light was used to excite surface plasmons on nanopillars. Reflected data was then normalized using a thick gold standard.

Conflict of Interest: The authors declare no competing financial interest.

Acknowledgment. This work was supported by the National Science Foundation Nanoscale Science and Engineering Center (NSEC) for High-rate Nanomanufacturing (NSF Grant 0832785). The experiments were conducted at the George J. Kostas Research Center at Northeastern University. We would like to thank Tae-Hoon Kim for his support in Atomic Force Microscopy measurements, David McKee for his support in substrate fabrication, C.Y. acknowledges Roger H. Grace for his financial support (R. H. Grace Fellowship). H.A. acknowledges the Office of Naval Research (11PR00755-00-P00001), the National Science Foundation (ECCS-0954790) and the Massachusetts Life Sciences Center. H.A. also acknowledges the DOD/Army Research Laboratory (Grant W911NF-06-2-0040) for supporting optical characterization facilities and biosafety laboratories at the Boston University Photonics Center.

Supporting Information Available: Detailed information (text, figures, and tables) about the electric field simulations, the dielectrophoretic force calculations, the control of directed assembly parameters and forces for the fabrication of 3-D nanostructures with precise dimensions, the mechanism of nanoparticle fusion into solid and homogeneous nanostructures, and material, electrical, and optical characterization of the fabricated 3-D nanostructures. This material is available free of charge via the Internet at <http://pubs.acs.org>.

REFERENCES AND NOTES

- Blackburn, J. M.; Long, D. P.; Cabanas, A.; Watkins, J. J. Deposition of Conformal Copper and Nickel Films from Supercritical Carbon Dioxide. *Science* **2001**, 294, 141–145.
- Wurtz, G. A.; Pollard, R.; Hendren, W.; Wiederrecht, G. P.; Gosztola, D. J.; Podolskiy, V. A.; Zayats, A. V. Designed Ultrafast Optical Nonlinearity in A Plasmonic Nanorod Metamaterial Enhanced by Nonlocality. *Nat. Nanotechnol.* **2011**, 6, 107–111.
- Fan, Z.; Razavi, H.; Do, J.-W.; Moriwaki, A.; Ergen, O.; Chueh, Y.-L.; Leu, P. W.; Ho, J. C.; Takahashi, T.; Reichert, L. A.; et al. Three-Dimensional Nanopillar-Array Photovoltaics on Low-Cost and Flexible Substrates. *Nat. Mater.* **2009**, 8, 648–653.
- Kabashin, A. V.; Evans, P.; Pastkovsky, S.; Hendren, W.; Wurtz, G. A.; Atkinson, R.; Pollard, R.; Podolskiy, V. A.; Zayats, A. V. Plasmonic Nanorod Metamaterials for Biosensing. *Nat. Mater.* **2009**, 8, 867–871.
- Grzelczak, M.; Vermant, J.; Furst, E. M.; Liz-Marzan, L. M. Directed Self-Assembly of Nanoparticles. *ACS Nano* **2010**, 4, 3591–3605.
- Velev, O. D.; Gupta, S. Materials Fabricated by Micro- and Nanoparticle Assembly—The Challenging Path from Science to Engineering. *Adv. Mater.* **2009**, 21, 1897–1905.
- Hermanson, K. D.; Lumsdon, S. O.; Williams, J. P.; Kaler, E. W.; Velev, O. D. Dielectrophoretic Assembly of Electrically Functional Microwires from Nanoparticle Suspensions. *Science* **2001**, 294, 1082–1086.
- Liberman, V.; Yilmaz, C.; Bloomstein, T. M.; Somu, S.; Echegoyen, Y.; Busnaina, A.; Cann, S. G.; Krohn, K. E.; Marchant, M. F.; Rothschild, M. A Nanoparticle Convective Directed Assembly Process for the Fabrication of Periodic Surface Enhanced Raman Spectroscopy Substrates. *Adv. Mater.* **2010**, 22, 4298–4302.
- Erb, R. M.; Son, H. S.; Samanta, B.; Rotello, V. M.; Yellen, B. B. Magnetic Assembly of Spherical Superstructures with Multipole Symmetry. *Nature* **2009**, 457, 999–1002.
- Zayats, M.; Kharitonov, A. B.; Pogorelova, S. P.; Lioubashevski, O.; Katz, E.; Willner, I. Probing Photoelectrochemical Processes in Au-CdS Nanoparticle Arrays by

- Surface Plasmon Resonance: Application for the Detection of Acetylcholine Esterase Inhibitors. *J. Am. Chem. Soc.* **2003**, *125*, 16006–16014.
11. Lee, H. J.; Yasukawa, T.; Suzuki, M.; Lee, S. H.; Yao, T.; Taki, Y.; Tanaka, A.; Kameyama, M.; Shiku, H.; Matsue, T. Simple and Rapid Preparation of Vertically Aligned Gold Nanoparticle Arrays and Fused Nanorods in Pores of Alumina Membrane Based on Positive Dielectrophoresis. *Sens. Actuators, B* **2009**, *136*, 320–325.
 12. Lee, H.; You, S.; Pikhitsa, P. V.; Kim, J.; Kwon, S.; Woo, C. G.; Choi, M. Three-Dimensional Assembly of Nanoparticles from Charged Aerosols. *Nano Lett.* **2011**, *11*, 119–124.
 13. Kraus, T.; Malaquin, L.; Schmid, H.; Riess, W.; Spencer, N. D.; Wolf, H. Nanoparticle Printing with Single-Particle Resolution. *Nat. Nanotechnol.* **2007**, *2*, 570–576.
 14. Min, Y.; Akbulut, M.; Kristiansen, K.; Golani, Y.; Israelachvili, J. The Role of Interparticle and External Forces in Nanoparticle Assembly. *Nat. Mater.* **2008**, *7*, 527–538.
 15. Ko, S. H.; Park, I.; Pan, H.; Grigoropoulos, C. P.; Pisano, A. P.; Luscombe, C. K.; Frechet, J. M. Direct Nanoimprinting of Metal Nanoparticles for Nanoscale Electronics Fabrication. *Nano Lett.* **2007**, *7*, 1869–1877.
 16. Pohl, H. A. *Dielectrophoresis*; Cambridge University Press: Cambridge, MA, 1978.
 17. Xiong, X.; Busnaina, A.; Selvarasah, S.; Somu, S.; Wei, M.; Mead, J.; Chen, C.-L.; Aceros, J.; Makaram, P.; Dokmeci, M. R. Directed Assembly of Gold Nanoparticle Nanowires and Networks for Nanodevices. *Appl. Phys. Lett.* **2007**, *91*, 063101.
 18. Bhatt, K. H.; Velev, O. D. Control and Modeling of the Dielectrophoretic Assembly of On-Chip Nanoparticle Wires. *Langmuir* **2004**, *20*, 467–476.
 19. Barsotti, R. J.; Vahey, M. D.; Wartena, R.; Chiang, Y.-M.; Voldman, J.; Stellacci, F. Assembly of Metal Nanoparticles into Nanogaps. *Small* **2007**, *3*, 488–499.
 20. Bhatt, K. H.; Grego, S.; Velev, O. D. An AC Electrokinetic Technique for Collection and Concentration of Particles and Cells on Patterned Electrodes. *Langmuir* **2005**, *21*, 6603–6612.
 21. Morgan, H.; Green, N. G. *AC Electrokinetics: Colloids and Nanoparticles*; Research Studies Press, Ltd.: Baldock, U.K., 2003.
 22. Bernard, L.; Calame, M.; Molen, S. J. v. d.; Liao, J.; Schönenberger, C. Controlled Formation of Metallic Nanowires via Au Nanoparticle AC Trapping. *Nanotechnology* **2007**, *18*, 235202.
 23. Tsong, T. T. Effects of An Electric Field in Atomic Manipulations. *Phys. Rev. B: Condens. Matter Mater. Phys.* **1991**, *44*, 13703–13710.
 24. Maugis, D.; Pollock, H. M. Surface Forces, Deformation and Adherence at Metal Microcontacts. *Acta Metall.* **1984**, *32*, 1323–1334.
 25. Ramsperger, U.; Uchihashi, T.; Nejoh, H. Fabrication and Lateral Electronic Transport Measurements of Gold Nanowires. *Appl. Phys. Lett.* **2001**, *78*, 85–87.
 26. Calleja, M.; Tello Ruiz, M.; Anguita, J. V.; Garca, F.; Garca Garca, R. Fabrication of Gold Nanowires on Insulating Substrates by Field-Induced Mass Transport. *Appl. Phys. Lett.* **2001**, *79*, 2471–2473.
 27. Zou, Z.; Kai, J.; Ahn, C. H. Electrical Characterization of Suspended Gold Nanowire Bridges with Functionalized Self-Assembled Monolayers Using a Top-Down Fabrication Method. *J. Micromech. Microeng.* **2009**, *19*, 055002.
 28. Durkan, C.; Welland, M. E. Size Effects in the Electrical Resistivity of Polycrystalline Nanowires. *Phys. Rev. B: Condens. Matter Mater. Phys.* **2000**, *61*, 14215–14218.
 29. Chappert, C.; Fert, A.; Van Dau, F. N. The Emergence of Spin Electronics in Data Storage. *Nat. Mater.* **2007**, *6*, 813–823.
 30. Tang, Z.; Kotov, N. A.; Giersig, M. Spontaneous Organization of Single CdTe Nanoparticles into Luminescent Nanowires. *Science* **2002**, *297*, 237–240.
 31. Menke, E. J.; Thompson, M. A.; Xiang, C.; Yang, L. C.; Penner, R. M. Lithographically Patterned Nanowire Electrodeposition. *Nat. Mater.* **2006**, *5*, 914–919.
 32. Chen, Y.-J.; Hsu, J.-H.; Lin, H.-N. Fabrication of Metal Nanowires by Atomic Force Microscopy Nanoscratching and Lift-Off Process. *Nanotechnology* **2005**, *16*, 1112–1115.
 33. Lane, M. W.; Murray, C. E.; McFeely, F. R.; Vereecken, P. M.; Rosenberg, R. Liner Materials for Direct Electrodeposition of Cu. *Appl. Phys. Lett.* **2003**, *83*, 2330–2332.
 34. Radisic, A.; Long, J. G.; Hoffmann, P. M.; Searson, P. C. Nucleation and Growth of Copper on TiN from Pyrophosphate Solution. *J. Electrochem. Soc.* **2001**, *148*, C41–C46.
 35. Emekli, U.; West, A. C. Effect of Additives and Pulse Plating on Copper Nucleation onto Ru. *Electrochim. Acta* **2009**, *54*, 1177–1183.
 36. Radisic, A.; Cao, Y.; Taephasitphongse, P.; West, A. C.; Searson, P. C. Direct Copper Electrodeposition on TaN Barrier Layers. *J. Electrochem. Soc.* **2003**, *150*, C362–C367.
 37. Park, K.-S.; Kim, S. Seedless Copper Electrodeposition onto Tungsten Diffusion Barrier. *J. Electrochem. Soc.* **2010**, *157*, D609–D613.
 38. Reid, J.; McKerrow, A.; Varadarajan, S.; Kozlowski, G. Copper Electroplating Approaches for 16nm Technology. *Solid State Technol.* **2010**, *53*, 14–17.
 39. Aydin, K.; Ferry, V. E.; Briggs, R. M.; Atwater, H. A. Broadband Polarization-Independent Resonant Light Absorption Using Ultrathin Plasmonic Super Absorbers. *Nat. Commun.* **2011**, *2*, 517.
 40. Lu, Y.-J.; Kim, J.; Chen, H.-Y.; Wu, C.; Dabidian, N.; Sanders, C. E.; Wang, C.-Y.; Lu, M.-Y.; Li, B.-H.; Qiu, X.; et al. Plasmonic Nanolaser Using Epitaxially Grown Silver Film. *Science* **2012**, *337*, 450–453.
 41. Boltasseva, A. Plasmonic Components Fabrication via Nanoimprint. *J. Opt. A: Pure Appl. Opt.* **2009**, *11*, 114001.
 42. Khademhosseini, B.; Biener, G.; Sencan, I.; Su, T. W.; Coskun, A. F.; Ozcan, A. Lensfree Sensing on A Microfluidic Chip Using Plasmonic Nanoapertures. *Appl. Phys. Lett.* **2010**, *97*, 221107.
 43. Yanik, A. A.; Huang, M.; Kamohara, O.; Artar, A.; Geisbert, T. W.; Connor, J. H.; Altug, H. An Optofluidic Nanoplasmonic Biosensor for Direct Detection of Live Viruses from Biological Media. *Nano Lett.* **2010**, *10*, 4962–4969.
 44. Cetin, A. E.; Coskun, A. F.; Galarreta, B. C.; Huang, M.; Herman, D.; Ozcan, A.; Altug, H. Handheld High-Throughput Plasmonic Biosensor Using Computational On-Chip Imaging. *Light: Sci. Appl.* **2014**, *3*, e122.
 45. Cetin, A. E.; Yanik, A. A.; Yilmaz, C.; Somu, S.; Busnaina, A.; Altug, H. Monopole Antenna Arrays for Optical Trapping, Spectroscopy, and Sensing. *Appl. Phys. Lett.* **2011**, *98*, 111110.
 46. Yilmaz, C.; Tae-Hoon, K.; Somu, S.; Busnaina, A. A. Large-Scale Nanorods Nanomanufacturing by Electric-Field-Directed Assembly for Nanoscale Device Applications. *IEEE Trans. Nanotechnol.* **2010**, *9*, 653–658.
 47. International Technology Roadmap for Semiconductors; Semiconductor Industry Association: Washington, D.C., 2011.
 48. Liu, X.; Zhu, J.; Jin, C.; Peng, L. M.; Tang, D.; Cheng, H. *In Situ* Electrical Measurements of Polytypic Silver Nanowires. *Nanotechnology* **2008**, *19*, 085711.
 49. Kai, W.; Ethan, S.; Paul, S.; Kenneth, B. C. Trapping and Rotating Nanoparticles Using A Plasmonic Nano-Tweezer with An Integrated Heat Sink. *Nat. Commun.* **2011**, *2*, 469–469.
 50. Liu, N.; Guo, H. C.; Fu, L. W.; Kaiser, S.; Schweizer, H.; Giessen, H. Three-Dimensional Photonic Metamaterials at Optical Frequencies. *Nat. Mater.* **2008**, *7*, 31–37.
 51. O'Carroll, D. M.; Fakonas, J. S.; Callahan, D. M.; Schierhorn, M.; Atwater, H. A. Metal-Polymer-Metal Split-Dipole Nanoantennas. *Adv. Mater.* **2012**, *24*, OP136–OP142.
 52. Wadell, C.; Antosiewicz, T. J.; Langhammer, C. Optical Absorption Engineering in Stacked Plasmonic Au-SiO(2)-Pd Nanoantennas. *Nano Lett.* **2012**, *12*, 4784–4790.
 53. Wu, Y.; Xiang, J.; Yang, C.; Lu, W.; Lieber, C. M. Single-Crystal Metallic Nanowires and Metal/Semiconductor Nanowire Heterostructures. *Nature* **2004**, *430*, 61–65.